Quantum error correction with metastable states of trapped ions using erasure conversion

Mingyu Kang,[1,2,*] Wesley C. Campbell,[3,4,5] and Kenneth R. Brown[1,2,6,7,†]

[1] *Duke Quantum Center, Duke University, Durham, NC 27701, USA*
[2] *Department of Physics, Duke University, Durham, NC 27708, USA*
[3] *Department of Physics and Astronomy, University of California, Los Angeles, CA 90095, USA*
[4] *Challenge Institute for Quantum Computation, University of California, Los Angeles, CA 90095, USA*
[5] *Center for Quantum Science and Engineering, University of California, Los Angeles, CA 90095, USA*
[6] *Department of Electrical and Computer Engineering, Duke University, Durham, NC 27708, USA*
[7] *Department of Chemistry, Duke University, Durham, NC 27708, USA*

(Dated: October 28, 2022)

Erasures, or errors with known locations, are a more favorable type of error for quantum error-correcting codes than Pauli errors. Converting physical noise into erasures can significantly improve the performance of quantum error correction. Here we apply the idea of performing erasure conversion by encoding qubits into metastable atomic states, proposed by Wu, Kolkowitz, Puri, and Thompson [Nat. Comm. **13**, 4657 (2022)], to trapped ions. We suggest an erasure-conversion scheme for metastable trapped-ion qubits and develop a detailed model of various types of errors. We then compare the logical performance of ground and metastable qubits on the surface code under various physical constraints and discuss the trade offs.

I. INTRODUCTION

Implementing quantum error correction (QEC) is a necessary path towards a scalable and fault-tolerant quantum computer, as quantum states are often inherently fragile and physical operations on quantum states have limited fidelities. QEC protects quantum information from errors by encoding a logical qubit into entangled states of multiple physical qubits [1].

There has been exciting efforts on manipulating and exploiting the *type* of physical error such that the performance of QEC is improved. One example is engineering qubits and operations that have strong bias between the X and Z Pauli noise [2–5] and designing QEC codes that benefit from such bias by achieving higher thresholds [6–12].

Another example is converting physical noise into *erasures*, i.e., errors with known locations [13–15]. It is clear that erasures are easier to correct than Pauli errors for QEC codes, as a code of distance d is guaranteed to correct at most $d-1$ erasures but only $\lfloor (d-1)/2 \rfloor$ Pauli errors.

Erasure conversion is performed by cleverly choosing the physical states encoded as qubits, such that physical noise causes leakage outside the qubit subspace. Crucially, such leakage should be detectable using additional physical operations [16–19]. Typically, undetected leakage errors can have even more detrimental effects on QEC than Pauli errors, as traditional methods for correcting Pauli errors do not apply [20] and methods such as leakage-reducing operations [21–23] and circuits [24–29] require significant overhead. However, when leakage errors are detectable, they can be converted to erasures by resetting the leaked qubit to a known state, e.g., the maximally-mixed state, within the qubit subspace. Erasure conversion is expected to achieve significantly higher QEC thresholds for hardware platforms such as superconducting qubits [19] and Rydberg atoms [18].

Trapped ions are leading candidate for a scalable quantum-computing platform [30]. In particular, QEC has been demonstrated in various trapped-ion experiments [31–36], which include fault-tolerant memory [34, 35] and even logical two-qubit gates [36] on distance-3 QEC codes. Here we address the question of whether the idea of erasure conversion can be applied to trapped-ion systems.

In fact, the erasure-conversion method in Ref. [18], designed for Rydberg atoms, can be directly applied to trapped ions. In Ref. [18], a qubit is encoded in the metastable level, such that the majority ($\sim 98\%$) of the Rydberg states' spontaneous decay during two-qubit gates does not return to the qubit subspace. Additional operations can detect such decay, thereby revealing the locations of errors. For trapped ions, the spontaneous decay of the excited states during laser-based gate operations is also the fundamental source of errors, which we aim to convert to erasures in this paper. Note that an earlier work [37] proposed a method of detecting a different type of error for trapped ions using qubits in the metastable level.

While the most popular choice of a trapped-ion qubit is the ground qubit encoded in the $S_{1/2}$ manifold, the metastable qubit encoded in the $D_{5/2}$ or $F^o_{7/2}$ manifold is also a promising candidate [38]. Recently, high-fidelity coherent conversion between ground and metastable qubits has been experimentally demonstrated using Yb^+ ions [39]. Also, it has been proposed that when ground and metastable qubits are used together, intermediate state measurement and cooling can be performed within

* mingyu.kang@duke.edu
† ken.brown@duke.edu

the same ion chain [38]. Therefore, it is a timely task to add erasure conversion to the list of functionalities of metastable qubits.

A careful analysis is needed before concluding that metastable qubits will be more advantageous in QEC than ground qubits. As will be discussed below, the erasure conversion relies on the fact that the excited states are more strongly coupled to the ground states than the metastable states. However, this fact may also cause the Rabi frequency of metastable qubits to be significantly smaller than that of ground qubits, which leads to longer gate time required for metastable qubits. Also, most metastable states decay to the ground manifold after a finite lifetime, while ground qubits have practically infinite lifetime. Whether the advantage of having higher threshold overcomes these drawbacks needs to be verified.

This paper is organized as follows. In Sec. II, we introduce the method of laser-based gate operation and erasure conversion on metastable qubits. In Sec. III, we show the model of various types of errors for ground and metastable qubits and discuss the criteria of comparison. In Sec. IV, we briefly introduce the surface code and the simulation method. In Sec. V, we present the results of comparing the QEC performance between ground and metastable qubits. Finally, we discuss the limitations of our simulations and future directions in Sec. VI.

II. ERASURE-CONVERSION SCHEME

In this paper we denote the hyperfine quantum state as $|L, J; F, M\rangle$, where L, J, F, and M are the quantum numbers in the standard notation. Also, we denote a set of all states with the same L and J as a manifold.

We define metastable qubit as hyperfine clock qubit encoded in the $D_{5/2}$ manifold, as suggested for Ba^+, Ca^+, and Sr^+ ions [38]. The qubit states are encoded as $|0\rangle_m := |2, 5/2; F_0, 0\rangle$ and $|1\rangle_m := |2, 5/2; F_0 + 1, 0\rangle$, such that the qubit is insensitive to magnetic field up to first order. Note that F_0 can be chosen as any integer that satisfies $|J - I| \leq F_0 < J + I$, where I is the nuclear spin.

Unlike ground qubits, metastable qubits are susceptible to idling error due to their finite lifetime. As a $D_{5/2}$ state spontaneously decays to the $S_{1/2}$ manifold, such error is a *leakage* outside the qubit subspace. The probability that idling error occurs during time duration t after state initialization is given by

$$p^{(\text{idle})}(t) = 1 - e^{-t/\tau_m}, \tag{1}$$

where τ_m is the metastable state's lifetime. Typically, τ_m is in the order of a few to tens of seconds for $D_{5/2}$ states [38].

Laser-based gate operations on metastable qubits are performed using the two-photon Raman transition, where the laser frequencies are detuned from the $D_{5/2} \to P_{3/2}$ transition by $-\Delta_m$. Apart from the "technical" sources of gate error due to noise in the experimental system, a fundamental source of gate error is the spontaneous scattering of the atomic state from the short-lived $P_{3/2}$ states. At the event of a $P_{3/2}$ state's decay, the state falls to one of the $S_{1/2}$, $D_{3/2}$, and $D_{5/2}$ manifolds with probability r_1, r_2, and r_3, respectively ($r_1 + r_2 + r_3 = 1$), where these probabilities are known as the *branching fractions*. Typically, r_1 is several times larger than r_2 and r_3.

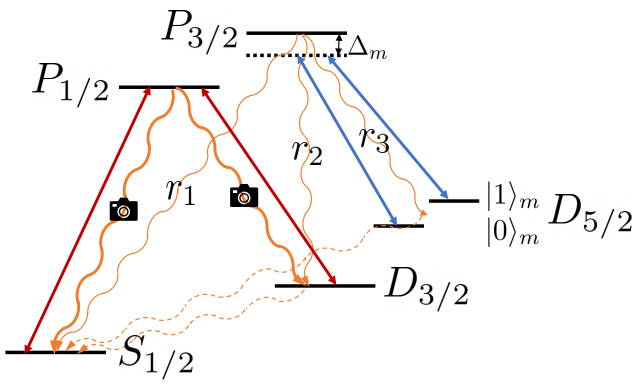

FIG. 1. Laser-based gate operation (blue) and leakage detection (red) on the $D_{5/2}$ metastable qubit. Orange curvy arrows show the paths of spontaneous decay. Gate operation uses two Raman beams detuned from the $D_{5/2} \to P_{3/2}$ transition by $-\Delta_m$. When a $P_{3/2}$ state decays, the state decays to one of the $S_{1/2}$, $D_{3/2}$, and $D_{5/2}$ manifolds with probability r_1, r_2, and r_3, respectively. Leakage detection detects the decay to the $S_{1/2}$ and $D_{3/2}$ manifolds using lasers that are resonant to the $S_{1/2} \to P_{1/2}$ and $D_{3/2} \to P_{1/2}$ transitions, which cause photons to scatter from the $P_{1/2}$ state and get collected.

If the atomic state decays to either qubit level of the $D_{5/2}$ manifold, the resulting gate error can be described as a *Pauli* error. On the other hand, if the atomic state decays to the $S_{1/2}$ manifold, or the $D_{3/2}$ manifold, or the hyperfine states of the $D_{5/2}$ manifold other than the qubit states, the resulting gate error is a *leakage*.

Similarly to the scheme proposed in Ref. [18], majority of the leakage can be detected. Specifically, whenever the atomic state has decayed to either $S_{1/2}$ or $D_{3/2}$ manifold, the state can be detected using lasers that induce fluorescence on cycling transitions resonant to $S_{1/2} \to P_{1/2}$ and to $D_{3/2} \to P_{1/2}$, as described in Fig. 1. Unlike a typical qubit-state detection scheme where the $|1\rangle$ state is selectively pumped into the $P_{1/2}$ manifold, this leakage detection can be performed using broadband lasers such that all hyperfine levels in the $S_{1/2}$ and $D_{3/2}$ manifolds are pumped.

At the rare event of detecting leakage, the qubit is reset to either $|0\rangle_m$ or $|1\rangle_m$, with probability 1/2 each. This effectively replaces the leaked state to the maximally-mixed state $I/2$ in the qubit subspace, which completes converting leakage to *erasure*. Resetting the metastable qubit can be performed by the standard ground-qubit state preparation followed by coher-

ent electric-quadrupole transition. This is recently experimentally demonstrated with high fidelity in less than 1 μs using Yb^+ ions [39].

Note that as transition between $P_{1/2}$ and $D_{5/2}$ states is forbidden, the photons fluoresced from the $P_{1/2}$ manifold during leakage detection and ground-qubit state preparation are not resonant to any transition with the metastable-qubit states involved. This allows the erasure conversion to be performed on an ion without destroying the nearby ions' qubit states with high probability. For ground qubits, an analogous erasure-conversion scheme of detecting leakage to the $D_{3/2}$ and $D_{5/2}$ manifolds will destroy the nearby ions' ground-qubit states, as both $P_{1/2}$ and $P_{3/2}$ states decay to $S_{1/2}$ states with high probability.

In the scheme described above, leakage to $D_{5/2}$ states other than the qubit states remains undetected. Such leakage can be handled by selectively pumping the $D_{5/2}$ hyperfine states except $|0\rangle_m$ and $|1\rangle_m$ to the $P_{3/2}$ manifold. With high probability, the atomic state eventually decays to either $S_{1/2}$ or $D_{3/2}$ manifold, which then can be detected as described above. However, this requires the laser polarization to be aligned with high precision such that the qubit states are not accidentally pumped [27]. Therefore, we defer a careful analysis on whether such process is feasible, and classify leakage to other $D_{5/2}$ states as undetected leakage when the erasure-conversion scheme is used.

III. TWO-QUBIT-GATE ERROR MODEL

In this section, we provide a detailed error model that will be used for comparing the logical performances of ground and metastable qubits. The source of gate errors we consider here is the spontaneous decay of excited states, which can cause various types of errors. When excited states decay back to one of the qubit states, either a bit flip or a phase flip occurs. When excited states decay to any other state, a leakage error occurs. Finally, for metastable qubits, when the state after decay is outside the $D_{5/2}$ manifold, such leakage can be converted to an erasure. Up to SubSec. III C, we calculate the rates of each type of error from atomic physics.

In our model, the only controllable parameter that determines the error rates is the lasers' detuning from the transition to excited states. In reality, the laser intensity is also important, as the gate time is determined by both detuning and laser intensity. In SubSec. III D, we provide methods of comparing ground and metastable qubits with fixed gate time, such that the errors due to technical noise are upper bounded to the same amount.

A. Definitions

In order to obtain equations for scattering rates that are valid for both ground and metastable qubits, we need to define several quantities. First, we define the maximal one-photon Rabi frequency of the transition between a state in the qubit states' manifold, denoted with subscript q, and an excited P state ($L = 1$), as

$$g_q := \frac{E_q}{2\hbar}\mu_q, \tag{2}$$

where

$$\mu_q := \sqrt{k_q}\left|\langle L=1||T^{(1)}(\boldsymbol{d})||L_q\rangle\right|. \tag{3}$$

Here, E_q is the electric-field amplitude of the laser used for qubit in manifold q, μ_q is the largest dipole-matrix element of transition between a state in manifold q and a P state, and $T^{(1)}(\boldsymbol{d})$ is the dipole tensor operator of rank one. Also, k_q is a coefficient that relates g_q to the *orbital* dipole transition-matrix element, which is calculated in Appendix A using the Wigner-3j and 6j coefficients.

Next, in order to obtain various types of scattering rates in the next section, we first define the decay rate of the excited states' manifold, denoted with subscript e, to the final (ground or metastable) manifold, denoted with subscript f, as

$$\begin{aligned}\gamma_{e,f} &:= \frac{\omega_{e,f}^3}{3\pi c^3\hbar\epsilon_0}\sum_{F_f,M_f}|\langle L_e,J_e;F_e,M_e|\boldsymbol{d}|L_f,J_f;F_f,M_f\rangle|^2\\ &= \alpha(L_e,J_e,L_f,J_f)\frac{\omega_{e,f}^3}{3\pi c^3\hbar\epsilon_0}\left|\langle L_e||T^{(1)}(\boldsymbol{d})||L_f\rangle\right|^2,\end{aligned} \tag{4}$$

where $\omega_{e,f}$ is the frequency difference between the excited and final states' manifolds. Also, $\alpha(L_e, J_e, L_f, J_f)$ is a coefficient that relates $\gamma_{e,f}$ to the *orbital* dipole transition-matrix element, which is calculated in Appendix A using the Wigner-3j and 6j coefficients. Note that $\gamma_{e,f}$ does not depend on F_e and M_e as the frequency differences between hyperfine states of the same manifold are ignored.

The laser-based gate operations use two-photon Raman beams that are detuned from the transition between manifolds e and q by $-\Delta_{e,q}$. In such case, the decay rate is given by

$$\gamma'_{e,f} := \gamma_{e,f}\left(\frac{\omega_{e,f}-\Delta_{e,q}}{\omega_{e,f}}\right)^3. \tag{5}$$

Note that $\omega_{e,f}-\Delta_{e,q}$ is determined by the laser frequency and does not depend on the choice of excited states' manifold e.

We use P states as excited states, i.e., $L_e = 1$. While J_e can be 1/2 or 3/2, (4) and (5) remove the dependence of $\gamma'_{e,f}/\alpha(L_e = 1, J_e, L_f, J_f)$ to J_e. This allows us to calculate the rates of scattering from $P_{1/2}$ and $P_{3/2}$ states only using γ'_f/α_f, where we define

$$\alpha_f := \alpha(L_e = 1, J_e = 3/2, L_f, J_f), \tag{6}$$

TABLE I. Values of the coefficient k_q (α_f), for various qubit (final) state's manifold.

	$q = S_{1/2}$	$q = D_{5/2}$		$f = S_{1/2}$	$f = D_{3/2}$	$f = D_{5/2}$
k_q	1/3	1/5	α_f	1/3	1/30	3/10

and calculate γ'_f from $P_{3/2}$ states. Specifically, combining (5) and the branching fractions of $P_{3/2}$ states, the rates of decay to the $S_{1/2}$, $D_{3/2}$, and $D_{5/2}$ manifolds are given by

$$\gamma'_f = \begin{cases} r'_1\gamma, & |f\rangle \in S_{1/2}, \\ r'_2\gamma, & |f\rangle \in D_{3/2}, \\ r'_3\gamma, & |f\rangle \in D_{5/2}, \end{cases} \tag{7}$$

where γ is the total decay rate of a $P_{3/2}$ state, and

$$\begin{aligned} r'_1 &:= (1 - \Delta_q/\omega_{P_{3/2},S_{1/2}})^3 \times r_1, \\ r'_2 &:= (1 - \Delta_q/\omega_{P_{3/2},D_{3/2}})^3 \times r_2, \\ r'_3 &:= (1 - \Delta_q/\omega_{P_{3/2},D_{5/2}})^3 \times r_3. \end{aligned} \tag{8}$$

Here, $-\Delta_q$ is the lasers' detuning from the transition between the qubit's manifold q and the $P_{3/2}$ manifold.

Table I shows the values of k_q (α_f) for various qubit (final) state's manifold, and their derivations can be found in Appendix A.

B. How errors arise from spontaneous scattering

Spontaneous scattering of the short-lived $P_{1/2}$ and $P_{3/2}$ states is the fundamental source of errors for laser-based gates. The type of error (phase-flip, bit-flip, leakage, erasure) depends on to which atomic state the short-lived states decay.

Rayleigh and Raman scattering are the two types of spontaneous scattering. Rayleigh scattering is the elastic case where the scattered photons and the atom do not exchange energy or angular momentum. Raman scattering is the inelastic case where the photons and the atom exchange energy, thus changing the atom's internal state. For Rayleigh scattering, the error occurs to the qubit only when the scattering rates differ between the two qubit states, which we call effective Rayleigh scattering. This results in the qubit's dephasing, or *phase-flip* ($\hat{Z}$) error. For Raman scattering, either *bit-flip* ($\hat{X}$ or $\hat{Y}$) or *leakage* error occurs. Finally, for metastable qubits, if the atomic state after Raman scattering is in either $S_{1/2}$ or $D_{3/2}$ manifold, the leakage can be detected and converted to *erasure*, as described in Sec. II.

The scattering rates can be calculated using the Kramers-Heisenberg formula as outlined in Ref. [40]. First, the effective Rayleigh scattering rate during the Raman transition of the qubit is given by

$$\Gamma^{(z)} = k_q g_q^2 \frac{\gamma'_q}{\alpha_q} \sum_\lambda \left(\sum_J A_{J,\lambda}^{1\to1} - \sum_{J'} A_{J',\lambda}^{0\to0} \right)^2, \tag{9}$$

where γ'_q is the decay rate to the qubit's manifold, $A_{J,\lambda}^{i\to j}$ is the scattering amplitude from $|i\rangle$ to $|j\rangle$ via excited state $|J\rangle$, λ is the polarization of the Raman beams, and 0 and 1 in the superscript denote the qubit states.

Similarly, the rate of Raman scattering that leads to bit-flip errors is given by [40, 41]

$$\Gamma^{(xy)} = k_q g_q^2 \frac{\gamma'_q}{\alpha_q} \sum_\lambda \left[\left(\sum_J A_{J,\lambda}^{0\to1} \right)^2 + \left(\sum_{J'} A_{J',\lambda}^{1\to0} \right)^2 \right], \tag{10}$$

and the rate of Raman scattering that leads to leakage errors is given by

$$\Gamma^{(l)} = k_q g_q^2 \sum_{f\neq0,1} \frac{\gamma'_f}{\alpha_f} \sum_\lambda \left[\left(\sum_J A_{J,\lambda}^{0\to f} \right)^2 + \left(\sum_{J'} A_{J',\lambda}^{1\to f} \right)^2 \right], \tag{11}$$

where $f \neq 0, 1$ denotes that $|f\rangle$ is not a qubit state. Finally, for $D_{5/2}$ metastable qubits with erasure conversion, the rate of Raman scattering that leads to erasures is given by

$$\Gamma^{(e)} = k_q g_q^2 \sum_{f\notin D_{5/2}} \frac{\gamma'_f}{\alpha_f} \sum_\lambda \left[\left(\sum_J A_{J,\lambda}^{0\to f} \right)^2 + \left(\sum_{J'} A_{J',\lambda}^{1\to f} \right)^2 \right], \tag{12}$$

where $f \notin D_{5/2}$ denotes that $|f\rangle$ is not in the $D_{5/2}$ manifold.

C. Two-qubit-gate error rates

We define ground qubit as hyperfine clock qubit encoded in the $S_{1/2}$ manifold as $|0\rangle_g := |0, 1/2; I - 1/2, 0\rangle$ and $|1\rangle_g := |0, 1/2; I + 1/2, 0\rangle$, where I is the nuclear spin. Raman beams for gate operations typically have frequencies between the $S_{1/2} \to P_{1/2}$ and $S_{1/2} \to P_{3/2}$ transition frequencies. The detuning from the $S_{1/2} \to P_{1/2}$ ($P_{3/2}$) transition is given by $\omega_F - \Delta_g$ ($-\Delta_g$), where ω_F is the frequency difference between the $P_{1/2}$ and $P_{3/2}$ manifolds. When the two Raman beams are both linearly polarized, the Rabi frequency of the qubit-state transition is given by [41, 42]

$$\Omega_g = \frac{g_g^2}{3} \left| \frac{\omega_F}{(\omega_F - \Delta_g)\Delta_g} \right|, \tag{13}$$

where g_g is the maximal one-photon Rabi frequency of a $S_{1/2}$ state.

Now we calculate the scattering rates in (9)-(11), where we replace the subscripts q with g. Also, $\gamma_g := r'_1\gamma$ as in (7). Assuming linearly-polarized Raman beams, the

rates are given by

$$\Gamma_g^{(z)} = 0, \tag{14}$$

$$\Gamma_g^{(xy)} = \frac{2}{9} r_1' \gamma g_g^2 \frac{\omega_F^2}{(\omega_F - \Delta_g)^2 \Delta_g^2}, \tag{15}$$

$$\Gamma_g^{(l)} = \frac{2}{9}\gamma \Big(\frac{g_g}{\Delta_g}\Big)^2 \Bigg[r_1' \frac{\omega_F^2}{(\omega_F - \Delta_g)^2} + 6 r_2' \frac{\omega_F^2 - 2\omega_F \Delta_g + 6\Delta_g^2}{(\omega_F - \Delta_g)^2} + 6 r_3' \Bigg], \tag{16}$$

where r_1', r_2', and r_3' are obtained by inserting $\Delta_q = \Delta_g$ into (8). Note that (14)-(16) are valid for any value of I.

The gate time for two-qubit gate following the Mølmer-Sørensen scheme [43] is typically given by

$$t_{\text{gate}} = \frac{\pi \sqrt{K}}{2\eta \Omega}, \tag{17}$$

where Ω is the qubit-state Rabi frequency, η is the Lamb-Dicke parameter, and K is the number of revolutions of the ions' trajectory in phase space [41]. Multiplying the scattering rate and the gate time gives the error rate. Therefore, inserting $\Omega = \Omega_g$ yields the phase-flip error rate $p_g^{(z)}$, the bit-flip error rate $p_g^{(xy)}$, the leakage rate $p_g^{(l)}$, and the total error rate p_g of each ground qubit on which two-qubit gate is applied as

$$p_g^{(z)} = 0, \tag{18}$$

$$p_g^{(xy)} = \frac{\pi \sqrt{K}}{3\eta} r_1' \gamma \left| \frac{\omega_F}{(\omega_F - \Delta_g)\Delta_g} \right|, \tag{19}$$

$$p_g^{(l)} = \frac{\pi \sqrt{K}}{3\eta} \frac{\gamma}{|\Delta_g|} \Bigg(r_1' \left| \frac{\omega_F}{\omega_F - \Delta_g} \right| + 6 r_2' \left| \frac{\omega_F^2 - 2\omega_F \Delta_g + 6\Delta_g^2}{(\omega_F - \Delta_g)\omega_F} \right| + 6 r_3' \left| \frac{\omega_F - \Delta_g}{\omega_F} \right| \Bigg), \tag{20}$$

$$p_g = p_g^{(z)} + p_g^{(xy)} + p_g^{(l)}. \tag{21}$$

We note that physically converting ground qubits' leakage to Pauli errors may be considered. Specifically, ground qubits' leakage to the $D_{3/2}$ and $D_{5/2}$ manifolds can be pumped back to the $S_{1/2}$ manifold, and leaked states in the $S_{1/2}$ manifold can be selectively pumped to the qubit states. While the former process is straightforward, the latter process suffers when the laser polarization is imperfect and unwanted (qubit) states are pumped [27]. Therefore, we assume for simplicity that for ground qubits, all leakage during gates remains as leakage.

Now we perform a similar analysis on metastable qubits, encoded as $|0\rangle_m := |2, 5/2; F_0, 0\rangle$ and $|1\rangle_m := |2, 5/2; F_0 + 1, 0\rangle$. We use linearly-polarized Raman beams detuned from the $D_{5/2} \to P_{3/2}$ transition by $-\Delta_m$, as described in Sec. II. The Rabi frequency is given by

$$\Omega_m = \frac{c_0 g_m^2}{|\Delta_m|}, \tag{22}$$

where g_m is the maximal one-photon Rabi frequency of a $D_{5/2}$ state, and c_0 is a geometric coefficient determined by I and F_0.

For metastable qubits, we calculate the scattering rates in (9)-(12), where we replace the subscripts q with m. Note that $\gamma_m := r_3' \gamma$ as in (7). The rates are given by

$$\Gamma_m^{(z)} = c_z r_3' \gamma \Big(\frac{g_m}{\Delta_m}\Big)^2, \tag{23}$$

$$\Gamma_m^{(xy)} = c_{xy} r_3' \gamma \Big(\frac{g_m}{\Delta_m}\Big)^2, \tag{24}$$

$$\Gamma_m^{(l)} = (c_1 r_1' + c_2 r_2' + c_l r_3') \gamma \Big(\frac{g_m}{\Delta_m}\Big)^2, \tag{25}$$

$$\Gamma_m^{(e)} = (c_1' r_1 + c_2 r_2') \gamma \Big(\frac{g_m}{\Delta_m}\Big)^2, \tag{26}$$

where r_1', r_2', and r_3' are obtained by inserting $\Delta_q = \Delta_m$ into (8), and c_z, c_{xy}, c_1, c_2, and c_l are geometric coefficients determined by I and F_0. Note that c_{xy} (c_l) comes from the Raman-scattering rates to the $D_{5/2}$ states within (outside) the qubit subspace. Also, c_1 (c_2) comes from the Raman-scattering rates to the $S_{1/2}$ ($D_{3/2}$) states.

Multiplying the rates to the gate time in (17) with $\Omega = \Omega_m$ yields the phase-flip error rate $p_m^{(z)}$, the bit-flip error rate $p_m^{(xy)}$, the leakage rate $p_m^{(l)}$, the erasure rate $p_m^{(e)}$, and the total error rate p_m of each metastable qubit on which two-qubit gate is applied as

$$p_m^{(z)} = \frac{\pi \sqrt{K}}{2\eta} \frac{c_z r_3'}{c_0} \frac{\gamma}{|\Delta_m|}, \tag{27}$$

$$p_m^{(xy)} = \frac{\pi \sqrt{K}}{2\eta} \frac{c_{xy} r_3'}{c_0} \frac{\gamma}{|\Delta_m|}, \tag{28}$$

$$p_m^{(l)} = \frac{\pi \sqrt{K}}{2\eta} \frac{c_1 r_1' + c_2 r_2' + c_l r_3'}{c_0} \frac{\gamma}{|\Delta_m|}, \tag{29}$$

$$p_m^{(e)} = \frac{\pi \sqrt{K}}{2\eta} \frac{c_1 r_1' + c_2 r_2'}{c_0} \frac{\gamma}{|\Delta_m|}, \tag{30}$$

$$p_m = p_m^{(z)} + p_m^{(xy)} + p_m^{(l)}. \tag{31}$$

We define $c_3 := c_z + c_{xy} + c_l$. Then, the ratio of the erasure rate to the total error rate is given by

$$R_e := \frac{p_m^{(e)}}{p_m} = \frac{c_1 r_1' + c_2 r_2'}{c_1 r_1' + c_2 r_2' + c_3 r_3'}, \tag{32}$$

which we denote as the *erasure-conversion rate* of metastable qubits, following the terminology of Ref. [18]. While R_e is a function of detuning Δ_m, at the limit $\Delta_m/\omega_F \to 0$, the erasure-conversion rate quickly approaches a constant value given by

$$R_e^{(0)} := \lim_{\frac{\Delta_m}{\omega_F} \to 0} R_e = \frac{c_1 r_1 + c_2 r_2}{c_1 r_1 + c_2 r_2 + c_3 r_3}. \tag{33}$$

TABLE II. Values of the nuclear spin I, the metastable state's lifetime τ_m [44, 45], the $P_{3/2}$ state's lifetime γ^{-1} [44, 46], the branching fractions [44, 47], the geometric coefficients, and the zero-detuning erasure-conversion rate $R_e^{(0)}$ of two metastable qubits chosen as examples.

Metastable qubit	I	τ_m	γ^{-1}	r_1	r_2	r_3	c_0	c_z	c_{xy}	c_1	c_2	c_l	$R_e^{(0)}$
$^{133}Ba^+$, $F_0=2$	1/2	30.14 s	6.2615 ns	0.7417	0.0280	0.2303	1/10	0	1/75	2/5	2/5	1/3	**0.7941**
$^{43}Ca^+$, $F_0=5$	7/2	1.16 s	6.924 ns	0.9347	0.0066	0.0587	$\sqrt{7/220}$	0.0035	7/165	29/55	29/55	0.3904	**0.9509**

Typically r_3 is a few times smaller than r_1, so the erasure-conversion rate is closer to one than to zero. Also, as Δ_m increases, r_3' decreases faster than r_1' [see (8)], so R_e becomes slightly larger than $R_e^{(0)}$.

We note that single-qubit-gate error rates can also be similarly obtained by inserting $\pi/2\Omega$ into the gate time. We do not consider single-qubit-gate errors in this paper as two-qubit gate errors are more than an order of magnitude larger, due to the additional factor $\sqrt{K}/\eta$.

D. Comparison of ground and metastable qubits

For comparing the logical performance of ground and metastable qubits, we consider the following three cases:

- Case I: $p_g = p_m$,
- Case II: $\Omega_g = \Omega_m$ and $E_g = E_m$,
- Case III: $\Omega_g = \Omega_m$ and $\Delta_g = \Delta_m$,

where E_g (E_m) is the electric-field amplitude of the laser used for ground (metastable) qubits.

In Case I, the total error rate is fixed between ground and metastable qubits, as in Ref. [18]. Here we expect metastable qubits to outperform ground qubits, as a significant portion (R_e) of metastable qubits' gate errors are erasures, which is more favorable than Pauli errors for QEC.

However, such comparison does not reflect an important disadvantage of metastable qubits. Namely, the transition between metastable and excited states is significantly weaker than that between ground and excited states, i.e., $\mu_m \ll \mu_g$. Therefore, given the same laser intensity, gates on metastable qubits require either smaller detuning [see (22)] or longer gate time [see (17)]. Note that R_e being close to one, which is an advantage of metastable qubits, also comes from the fact that $\mu_m \ll \mu_g$, as will be seen in detail below.

If we completely ignore noise in the experimental system, one can simply use sufficiently longer gate time for metastable qubits than for ground qubits, such that the total error rates due to spontaneous scattering match. However, this is unrealistic, especially given that the dominant sources of two-qubit-gate errors in the current state-of-the-art trapped-ion systems are motional heating and motional dephasing [48–50], whose effects build up with gate time.

Therefore, we also compare ground and metastable qubits with fixed Rabi frequency, i.e., $\Omega_g = \Omega_m$. This requires smaller detuning for metastable qubits, which leads to larger gate error due to spontaneous scattering for metastable qubits. However, the gate time is fixed, so the gate error due to technical noise is upper bounded to the same amount.

We note in passing that with metastable qubits and the erasure-conversion scheme, decreasing the detuning Δ_m is in some sense converting Pauli errors to erasures (and small amount of undetected leakage), as the gate time decreases at the cost of larger spontaneous-scattering rate. Given the magnitude of technical noise, an optimal amount of detuning should exist, where the optimum is determined by the *logical* error rate (see Ref. [51] for a similar approach).

To fix the Rabi frequencies, we first express the ratio μ_m/μ_g using variables with experimentally known values. From (3) and (4), we have

$$\left(\frac{\mu_m}{\mu_g}\right)^2 = \frac{k_m \alpha_g \gamma_{e,m}}{k_g \alpha_m \gamma_{e,g}} \left(\frac{\omega_{e,g}}{\omega_{e,m}}\right)^3 = \frac{2r_3}{3r_1}\left(\frac{\omega_{e,g}}{\omega_{e,m}}\right)^3, \quad (34)$$

where $\omega_{e,g}$ ($\omega_{e,m}$) is the frequency difference between the $P_{3/2}$ and $S_{1/2}$ ($D_{5/2}$) manifolds. Note that r_3/r_1 is proportional to $(\mu_m/\mu_g)^2$, which shows that large R_e stems from $\mu_m \ll \mu_g$.

Then, the Rabi-frequency ratio Ω_m/Ω_g is obtained by (2), (13), and (22) as

$$\begin{aligned}\frac{\Omega_m}{\Omega_g} &= 3c_0 \left|\frac{(\omega_F - \Delta_g)\Delta_g}{\omega_F \Delta_m}\right| \left(\frac{\mu_m E_m}{\mu_g E_g}\right)^2, \\ &= 2c_0 \frac{r_3}{r_1} \left|\frac{(\omega_F - \Delta_g)\Delta_g}{\omega_F \Delta_m}\right| \left(\frac{\omega_{e,g}}{\omega_{e,m}}\right)^3 \left(\frac{E_m}{E_g}\right)^2. \quad (35)\end{aligned}$$

The condition $\Omega_m/\Omega_g = 1$ will be used for comparing ground and metastable qubits with fixed gate time. There are two additional choices of fixing variables: $E_g = E_m$ (Case II) and $\Delta_g = \Delta_m$ (Case III). In Case II, the ratio of detunings is given by

$$\text{Case II}: \quad \frac{\Delta_m}{\Delta_g} = 2c_0 \frac{r_3}{r_1} \left|1 - \frac{\Delta_g}{\omega_F}\right| \left(\frac{\omega_{e,g}}{\omega_{e,m}}\right)^3, \quad (36)$$

which is typically in the order of 10^{-1} unless Δ_g is close to ω_F. In Case III, the ratio of electric-field amplitudes

is given by

$$\text{Case III}: \quad \frac{E_m}{E_g} = \sqrt{\frac{r_1}{2c_0 r_3}} \left|1 - \frac{\Delta_g}{\omega_F}\right|^{-1/2} \left(\frac{\omega_{e,m}}{\omega_{e,g}}\right)^{3/2}, \tag{37}$$

which is typically several times larger than one unless $\Delta_g = \Delta_m$ is close to ω_F.

We note that Case III, where E_m is larger than E_g, is experimentally motivated, as the limitation on laser intensity is often imposed by material loss in optical devices such as mirrors and waveguides [52]. Such loss is less severe with longer laser wavelength. As the $D_{5/2} \to P_{3/2}$ transition has longer wavelength than the $S_{1/2} \to P_{3/2}$ transition, we expect that using metastable qubits allows significantly larger laser intensity for gate operations than using ground qubits.

IV. SURFACE-CODE SIMULATION

In order to compare the circuit-level performance of ground qubits and metastable qubits equipped with erasure conversion in QEC, we simulate the surface code [53–55] (see Ref. [55] for a detailed review). In particular, we consider the rotated surface code [56], which uses slightly fewer qubits than the standard surface code. Figure 2(a) shows the rotated surface code of distance $d = 3$ consisting of $2d^2 - 1 = 17$ qubits. The logical qubit is encoded in d^2 data qubits (black circles), and the Z and X stabilizers (red and blue plaquettes, respectively) are measured using $d^2 - 1$ syndrome qubits (white circles). The logical operator $\hat{Z}_L$ ($\hat{X}_L$) is the product of the $\hat{Z}$ ($\hat{X}$) operators of d data qubits across a horizontal (vertical) line. The measured stabilizers are used by a decoder in inferring the locations and types ($\hat{X}$, $\hat{Y}$, or $\hat{Z}$) of errors.

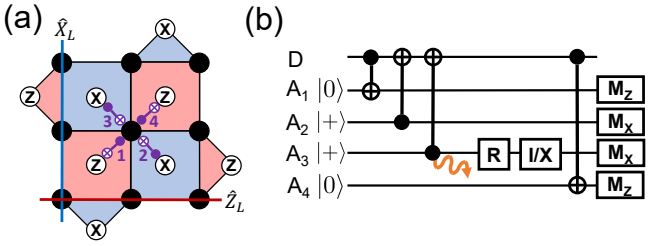

FIG. 2. (a) Layout of the rotated surface code of distance $d = 3$. Black (white) circles represent data (syndrome) qubits. Red (blue) plaquettes represent Z (X) stabilizers. Red horizontal (blue vertical) line represents logical $\hat{Z}_L$ ($\hat{X}_L$) operator. CNOT gates between a data qubit and corresponding syndrome qubits are applied in the numbered order. (b) Quantum circuit for a single round of error correction. Here we show an example where the third syndrome qubit is leaked and then converted to the maximally mixed state by erasure conversion. R denotes resetting the qubit to $|0\rangle$. I/X denotes that either $\hat{I}$ or $\hat{X}$ gate is applied with probability 1/2 each. M_Z (M_X) denotes qubit-state measurement in the Z (X) basis.

The surface code is a viable candidate for QEC in an experimental system, as it has high ($\sim 1\%$) circuit-level threshold and can be implemented using only nearest-neighbor interactions on a two-dimensional layout. Recently there has been wide experimental success in demonstrating fault-tolerant memory of a single logical qubit encoded in the surface code using superconducting qubits [57–59].

We note that for trapped-ion systems, using nearest-neighbor interactions is not required. Thus, recent QEC experiments in trapped-ion systems have used the Bacon-Shor code [34], the five-qubit code [36], and the color code [35, 36]. For distance $d = 3$, these codes allow fewer number of physical qubits and gate operations [60]. However, simulating the error-correction threshold using these codes can be complicated, as the family of each code of various distances is defined using code concatenation (see Ref. [61] for an example of the color code).

Meanwhile, the family of rotated surface codes is straightforwardly defined such that a code of distance d uses d^2 data qubits and $d^2 - 1$ syndrome qubits. Therefore, for the purpose of comparing the performance of ground and metastable qubits in QEC, we choose to simulate the rotated surface codes. We expect similar results for other codes as well, as long as the decoder can use the information on the erasure locations.

Figure 2(b) shows the circuit for a single round of error correction for surface codes. First, the syndrome qubits for measuring the Z (X) stabilizers are initialized to state $|0\rangle$ ($|+\rangle$). Then, four CNOT gates are performed between the data qubit and the syndrome qubits, in the correct order. Finally, the syndrome qubits are measured in the respective basis to provide the error syndromes. This circuit is performed on all data qubits in parallel. As the measurements can be erroneous as well, typically d rounds of error correction are consecutively performed for a distance-d code.

The most probable set of errors that could have caused the observed syndromes is inferred by a decoder run by a classical computer. Among the various efficient decoders for surface codes [62–64], we choose the minimum-weight perfect-matching (MWPM) decoder, which finds the error chain of minimum weight using Edmonds' algorithm [62]. The errors are corrected by simply keeping track of the Pauli frame, thus not requiring any physical gate operations [55].

Erasure conversion on metastable qubits is performed by replacing a leaked qubit to the maximally mixed state whenever leakage is detected. In the actual implementation, this can be done by resetting the leaked qubit to $|0\rangle_m$ and then performing a $\hat{X}$ gate with probability 1/2, as shown on the third syndrome qubit of Fig. 2(b). The decoder uses the information on the erasure locations by setting the weight of erased data qubits to zero, which decreases the weights of error chains consisting of the erased data qubits.

To evaluate the QEC performance, we simulate the logical memory of rotated surface codes in the Z basis.

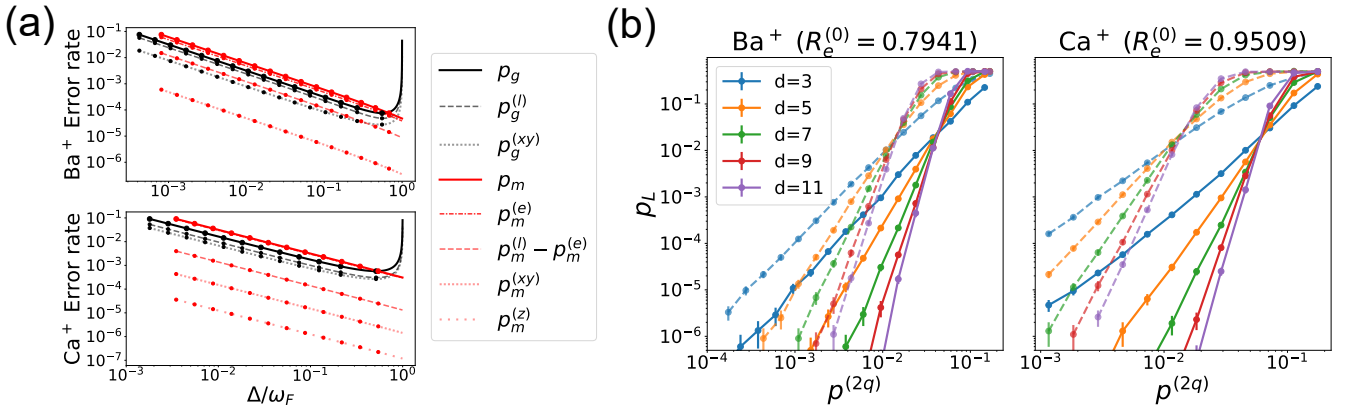

FIG. 3. (a) Error rates of various types as the detuning from the $P_{3/2}$ manifold is varied. Plots for Ba^+ (top) and Ca^+ (bottom) ion qubits in Table II are shown. For ground (metastable) qubits, $p_g^{(l)}$ ($p_m^{(e)}$) most significantly contributes to p_g (p_m). For Ca^+, the p_m and $p_m^{(e)}$ curves are hardly distinguishable. Also note that metastable qubits require larger detuning than ground qubits in order to have the same total error rate. (b) Logical error rates of ground (dashed) and metastable (solid) qubits for various code distances d and two-qubit-gate error rates $p^{(2q)} = 2p - p^2$, where $p = p_g = p_m$ as in Case I. The error rates marked as points in (a) are used in simulations. The error bars represent the 95% confidence interval. The thresholds, determined by intersections of the curves for d =5 to 11, are 1.49%, 4.36%, 1.48%, and 6.13% for ground Ba^+, metastable Ba^+, ground Ca^+, and metastable Ca^+ qubits, respectively.

Specifically, we initialize the data qubits to $|0\rangle$, perform d rounds of error correction for the distance-d code, and then measure the data qubits in the Z basis. Whether a logical error occurred is determined by comparing the measurement of the $\hat{Z}_L$ operator [see Fig. 2(a)] and the expected value of $\hat{Z}_L$ after decoding. This is repeated many times to determine the logical error rate.

The circuit-level simulations in this paper are performed using "Stim" [65], a software package for fast simulations of quantum stabilizer circuits. The error syndromes generated by the circuit simulations are decoded using "PyMatching" [66], a software package that executes the MWPM decoder. In particular, Stim allows simulating erasures and feeding the location information into the decoder [67].

V. RESULTS

In this paper we choose two ion species, Ba^+ and Ca^+, as examples for $D_{5/2}$ metastable qubits. For each species, we choose the isotope and F_0, the hyperfine total angular-momentum number of $|0\rangle_m$, such that the qubit-splitting frequency is the largest among the candidates shown in Ref. [38]. The chosen isotopes and F_0 are $^{133}Ba^+$, $F_0 = 2$ and $^{43}Ca^+$, $F_0 = 5$.

Table II shows the values of the metastable state's lifetime τ_m [44, 45], the $P_{3/2}$ state's lifetime γ^{-1} [44, 46], the branching fractions [44, 47], the geometric coefficients, and the zero-detuning erasure-conversion rate $R_e^{(0)}$ of the two chosen metastable qubits. The metastable qubit's error rates in (27) - (31) are estimated using these values. Notably, for both qubits, $R_e^{(0)}$ is slightly larger than $r_1 + r_2$, which is the erasure-conversion rate that can be naively estimated from Fig. 1.

In our simulations, the detuning from the $P_{3/2}$ manifold Δ_g (Δ_m) is the only knob used to vary the physical error rates of the ground (metastable) qubits, as $\eta = 0.05$ and $K = 1$ are fixed to their typical values. Figure 3(a) shows the chosen Ba^+ and Ca^+ qubits' error rates of various types as the detuning is varied. For ground (metastable) qubits, undetected-leakage (erasure) rate takes the largest portion of the total error rate. Although indistinguishable from the plot, from left to right of the detunings marked as points, the erasure-conversion rate $R_e := p_m^{(e)}/p_m$ is varied from 0.7941 to 0.8032 for Ba^+ and from 0.9509 to 0.9517 for Ca^+.

We note that for ground qubits, Δ_g is typically set such that the Raman beams are far detuned from both $P_{1/2}$ and $P_{3/2}$ manifolds, in order to minimize the detrimental leakage error due to the spontaneous scattering. However, for metastable qubits, smaller detuning may be considered to increase the Rabi frequency and thus decrease the effects of technical noise that build up with gate time, as significant amount of leakage errors may be converted to erasures.

First, we use the error model where the spontaneous scattering during two-qubit gate is the only source of error. The simulated error rates of each type are given by the points in Fig. 3(a). Both undetected leakage and erasure of rate p are simulated as depolarizing error, i.e., Pauli error randomly chosen from $\{\hat{I}, \hat{X}, \hat{Y}, \hat{Z}\}$ with probability $p/4$ each. In the simulations, the only difference between undetected leakage and erasure is that the decoder knows and uses the locations of erasures but not the locations of undetected leakage. The errors during single-qubit gates, state preparation, idling, and measurement

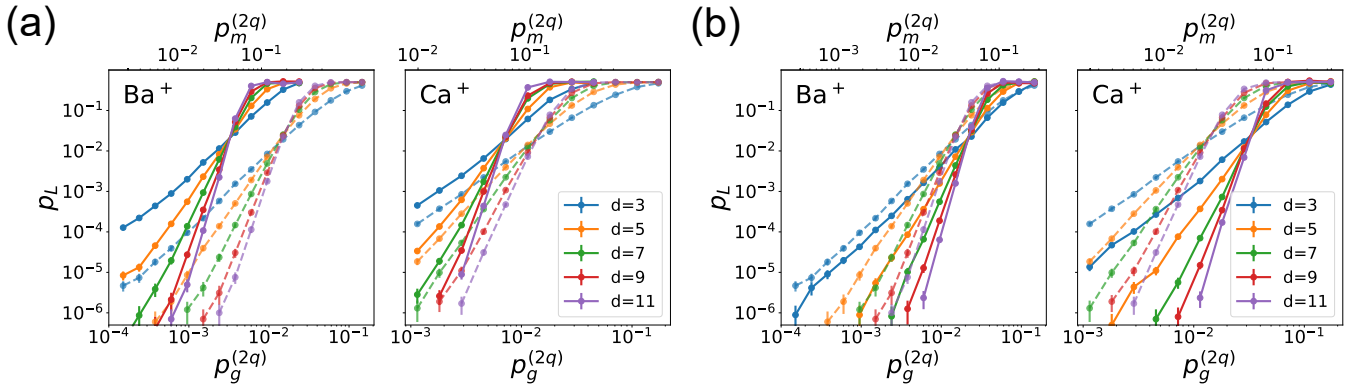

FIG. 4. Logical error rates of ground (dashed) and metastable (solid) qubits for various code distances d and two-qubit-gate error rates. Idling (measurement) errors of fixed rate are added for metastable (both) qubits. The error bars represent the 95% confidence interval. (a) Ground and metastable qubits' two-qubit-gate error rates $p_g^{(2q)}$ and $p_m^{(2q)}$ are aligned with respect to Case II: $\Omega_g = \Omega_m$ and $E_g = E_m$. From left to right of the region where both ground and metastable qubits' logical error rates are plotted, the ratio of detunings Δ_m/Δ_g given by (36) is varied from 0.0681 to 0.152 for Ba^+ and from 0.111 to 0.229 for Ca^+. For Case II, ground qubits outperform metastable qubits. (b) Ground and metastable qubits' two-qubit-gate error rates $p_g^{(2q)}$ and $p_m^{(2q)}$ are aligned with respect to Case III: $\Delta_g = \Delta_m$. To match the Rabi frequencies ($\Omega_g = \Omega_m$), from left to right of the plotted region, the ratio of electric-field amplitudes E_m/E_g given by (37) is varied from 3.83 to 2.56 for Ba^+ and from 3.00 to 2.09 for Ca^+. For Case III, metastable qubits outperform ground qubits. For both (a) and (b), the top horizontal axes are not exactly at log scale.

are not considered.

We assume that during a two-qubit gate, an error on one of the two qubits does not propagate to the other qubit. This is motivated from the fact that (i) most of the errors are (detected or undetected) leakage errors, and (ii) when a two-qubit-gate operation following the Mølmer-Sørensen scheme is performed between a qubit and an ion in a leaked state, the resulting operation on the qubit is simply the identity. We note that Ref. [68] provides a detailed analysis on how Pauli errors during a two-qubit gate propagate.

Figure 3(b) shows the logical error rates of ground (dashed) and metastable (solid) qubits for various code distances and two-qubit-gate error rates $p^{(2q)}$. Here, $p^{(2q)} := 2p - p^2$, where $p = p_g = p_m$ as in Case I. As expected from Ref. [18], using erasure conversion on metastable qubits significantly improves the threshold, which leads to dramatic reduction in the logical error rates, compared to using ground qubits. The thresholds for our error model and the MWPM decoder are determined by intersections of the curves for d =5, 7, 9, and 11. For Ba^+ ion, which has $R_e^{(0)} = 0.7941$, the threshold improves from 1.49% to 4.36% when metastable qubits are used. For Ca^+ ion, which has $R_e^{(0)} = 0.9509$, the threshold improves from 1.48% to 6.13%. A close inspection of the plot shows that for Ca^+ ion, with a fixed value of d, the slope below the threshold is steeper for metastable qubits than for ground qubits, which indicates that erasure conversion improves the *effective code distance* as well [18].

While these results are promising, the disadvantages of metastable qubits are not yet reflected. The shorter lifetimes of metastable qubits are not considered. Also, Fig. 3(a) shows that in order to achieve a fixed error rate (Case I), metastable qubits require larger detuning than ground qubits, which leads to smaller Rabi frequency and longer gate time.

In the following simulations, we add idling errors of metastable qubits into the error model. Specifically, for a surface-code cycle time T, we assume that *all* metastable qubits have an additional probability of erasure $p^{(\mathrm{idle})}(T)/4$ [see (1)] before each layer of CNOT gates, where the factor of 1/4 comes from that each error-correction round consists of four layers of CNOT gates. Here we assume $T = 3$ ms, considering the time required for the state-of-the-art sideband cooling [69]. For Ba^+ (Ca^+) ion, the idling error rate is fixed to $p^{(\mathrm{idle})}(T)/4 = 2.49 \times 10^{-5}$ (6.46×10^{-4}). The QEC performance of metastable qubits for various values of idling-error rates is discussed in Appendix B. We also add measurement errors of fixed rate 10^{-4}, which is roughly the state-of-the-art for trapped ions [70, 71], for both ground and metastable qubits.

Figure 4(a) shows the comparison result for Case II. The top and bottom horizontal axes represent the ground and metastable qubits' two-qubit-gate error rates $p_g^{(2q)} := 2p_g = p_g^2$ and $p_m^{(2q)} := 2p_m - p_m^2$, respectively. For each $p_g^{(2q)}$, the vertically aligned $p_m^{(2q)}$ is determined by the ratio of detunings Δ_m/Δ_g that satisfies the conditions $\Omega_g = \Omega_m$ and $E_g = E_m$ [see (36)]. As a result, from the lowest to highest simulated $p_m^{(2q)}$, Δ_m/Δ_g is varied from 0.0681 to 0.152 for Ba^+ ion and from 0.111 to 0.229 for Ca^+ ion. Thus, each $p_m^{(2q)}$ is compared with an order of magnitude lower $p_g^{(2q)}$. In this case, for both

Ba^+ and Ca^+ ions, ground qubits outperform metastable qubits, despite having lower thresholds. The effects of idling and measurement errors are negligible in the range of two-qubit-gate errors simulated here.

Figure 4(b) shows the comparison result for Case III. Here, $p_g^{(2q)}$ and $p_m^{(2q)}$ that are vertically aligned correspond to the same detuning ($\Delta_g = \Delta_m$). Thus, each $p_m^{(2q)}$ is compared with at most two times lower $p_g^{(2q)}$, which can be overcome by the improvement in the threshold due to erasure conversion. For both Ba^+ and Ca^+ ions, metastable qubits outperform ground qubits. The advantage of metastable qubits is larger for Ca^+, due to the larger erasure-conversion rate. Again, the effects of idling and measurement errors are negligible.

For Case III, to achieve both $\Omega_g = \Omega_m$ and $\Delta_g = \Delta_m$, from the lowest to highest simulated error rates, E_m/E_g is varied from 3.83 to 2.56 for Ba^+ ion and from 3.00 to 2.09 for Ca^+ ion [see (37)]. Therefore, in order to achieve the advantage shown in Fig. 4(b), metastable qubits require larger laser intensity than ground qubits. We emphasize that it is reasonable to assume metastable qubits allow larger laser intensity for gate operations, as material loss due to lasers is less severe for longer laser wavelength. In reality, the advantage of metastable qubits may depend on achievable laser intensities.

VI. CONCLUSION AND OUTLOOK

In this paper, we showed that trapped-ion metastable qubits equipped with erasure conversion can outperform ground qubits in fault-tolerant logical memory using surface codes. Even when the Rabi frequency is fixed between ground and metastable qubits, metastable qubits' logical error rates are lower when reasonably larger laser intensity is allowed (such that detuning from the $P_{3/2}$ manifold is the same). We hope that this paper motivates further research in using metastable trapped-ion qubits for scalable and fault-tolerant quantum computing [38]. Also, the methodology of using our detailed error model for comparing ground and metastable qubits may be applied back to the Rydberg-atom platform [18].

While this work may serve as a proof of principle, it has several limitations that lead to future directions. First, undetected-leakage errors are simulated as depolarizing errors. In reality, fault-tolerantly handling leakage errors requires significant overhead, such as leakage-reducing operations [21–23] and circuits [24–29]. In particular, the trade offs of using leakage-reducing circuits on trapped-ion ground qubits have been discussed in Refs. [27, 28]. When the cost of mitigating leakage is considered, we expect the advantage of using metastable qubits to be significantly larger, as undetected leakage is the dominant type of error for ground qubits but not for metastable qubits equipped with erasure conversion.

Second, we do not consider errors due to miscalibration of the physical parameters, which may cause overrotation errors. This is important because (i) overrotation error is often larger than stochastic error for state-of-the-art two-qubit gates [49, 50], and (ii) calibrating physical parameters to high precision may require large number of shots and long experiment time [72].

Notably, overrotation errors can be converted to erasures using certified quantum gates on metastable qubits [37]. In this gate scheme, auxiliary states outside the qubit subspace are used, such that overrotation causes residual occupation of the auxiliary states, which can be detected by optical pumping. While Ref. [37] considers a heralded gate of success probability smaller than one, in the perspective of QEC, this is essentially erasure conversion. More work needs to be done on generalizing certified quantum gates to other encodings of qubit states and to more commonly-used two-qubit-gate schemes such as the Mølmer-Sørensen scheme.

Finally, we only consider the examples of $D_{5/2}$ metastable qubits, which have limited lifetime (see Table II). Meanwhile, Yb^+ ion's metastable qubit encoded in the $F^o_{7/2}$ manifold is even more promising, as its lifetime is as long as several days to years [38]. The laser-based gate operations on such metastable qubit may use excited states that are more "exotic" than the P states. We hope this work motivates future research on utilizing these exotic states, as well as measuring their properties such as decay rates and branching fractions.

ACKNOWLEDGMENTS

M.K. thanks Craig Gindey for his advice on using Stim and thanks Shilin Huang for helpful discussions. W.C.C. acknowledges support from NSF grant no. PHY-2207985 and ARO grant no. W911NF-20-1-0037. M.K. and K.R.B acknowledge support from the Office of the Director of National Intelligence, Intelligence Advanced Research Projects Activity through ARO Contract W911NF-16-1-0082 and the NSF sponsored Quantum Leap Challenge Institute for Robust Quantum Simulation grant no. OMA-2120757.

APPENDIX A: Derivations of k_q and α_f

In this appendix we calculate the coefficients k_q and α_f, introduced in (3), (4), and (6), using the Wigner $3j$ and $6j$ symbols. We mainly use two relations. First is the relation between the hyperfine transition element and the fine-structure-level transition element, given by

$$\langle L_a, J_a; F_a, M_a|T^{(1)}_\lambda(\boldsymbol{d})|L_b J_b; F_b, M_b\rangle = (-1)^{F_a - M_a + J_a + I + F_b + 1}\sqrt{(2F_a+1)(2F_b+1)}\begin{pmatrix} F_a & 1 & F_b \\ -M_a & s & M_b\end{pmatrix} \times \begin{Bmatrix} J_a & F_a & I \\ F_b & J_b & 1\end{Bmatrix}\langle L_a, J_a||T^{(1)}(\boldsymbol{d})||L_b, J_b\rangle, \tag{A1}$$

where λ is the photon polarization. Next is the relation between the fine-structure-level transition element and the orbital transition element, given by

$$\langle L_a, J_a||T^{(1)}(\boldsymbol{d})||L_b, J_b\rangle = (-1)^{(L_a + \frac{1}{2} + J_b + 1)}\sqrt{(2J_a+1)(2J_b+1)}\begin{Bmatrix} L_a & J_a & S \\ J_b & L_b & 1\end{Bmatrix}\langle L_a||T^{(1)}(\boldsymbol{d})||L_b\rangle, \tag{A2}$$

where $S = 1/2$ is the electron spin.

We first calculate k_q. The largest dipole-matrix element of transition between a state in manifold q and a P state is given by

$$\mu_q := \langle 1, \frac{3}{2}; I + \frac{3}{2}, I + \frac{3}{2}|T^{(1)}_{\frac{3}{2} - J_q}(\boldsymbol{d})|L_q, J_q; I + J_q, I + J_q\rangle, \tag{A3}$$

where I is the nuclear spin, which we assume to be a half integer. Applying (A1) and (A2) sequentially, we obtain

$$\begin{aligned}\mu_q &= (-1)^{J_q + 2I + \frac{1}{2}}\sqrt{(2I+4)(2I+2J_q+1)}\begin{pmatrix} I+\frac{3}{2} & 1 & I+J_q \\ -I-\frac{3}{2} & \frac{3}{2}-J_q & I+J_q\end{pmatrix} \\ &\quad\times\begin{Bmatrix} \frac{3}{2} & I+\frac{3}{2} & I \\ I+J_q & J_q & 1\end{Bmatrix}\langle L=1, J=\frac{3}{2}||T^{(1)}(\boldsymbol{d})||L_q, J_q\rangle \\ &= (-1)^{2J_q+2I+1}\sqrt{(2I+4)(2I+2J_q+1)(4)(2J_q+1)} \\ &\quad\times\begin{pmatrix} I+\frac{3}{2} & 1 & I+J_q \\ -I-\frac{3}{2} & \frac{3}{2}-J_q & I+J_q\end{pmatrix}\begin{Bmatrix} \frac{3}{2} & I+\frac{3}{2} & I \\ I+J_q & J_q & 1\end{Bmatrix}\begin{Bmatrix} 1 & \frac{3}{2} & \frac{1}{2} \\ J_q & L_q & 1\end{Bmatrix}\langle L=1||T^{(1)}(\boldsymbol{d})||L_q\rangle.\end{aligned} \tag{A4}$$

For ground qubits ($q = g$), inserting $L_q = 0$ and $J_q = \frac{1}{2}$ to (A4) gives

$$\begin{aligned}\mu_g &= (-1)^{2I}\sqrt{(2I+4)(2I+2)(4)(2)} \\ &\quad\times\begin{pmatrix} I+\frac{3}{2} & 1 & I+\frac{1}{2} \\ -I-\frac{3}{2} & 1 & I+\frac{1}{2}\end{pmatrix}\begin{Bmatrix} \frac{3}{2} & I+\frac{3}{2} & I \\ I+\frac{1}{2} & \frac{1}{2} & 1\end{Bmatrix}\begin{Bmatrix} 1 & \frac{3}{2} & \frac{1}{2} \\ \frac{1}{2} & 0 & 1\end{Bmatrix}\langle L=1||T^{(1)}(\boldsymbol{d})||L_g=0\rangle \\ &= (-1)^{2I}\sqrt{(2I+4)(2I+2)(4)(2)}\times\frac{1}{\sqrt{2I+4}}\frac{(-1)^{2I+1}}{\sqrt{(2I+2)(4)}}\frac{(-1)}{\sqrt{6}}\langle L=1||T^{(1)}(\boldsymbol{d})||L_g=0\rangle \\ &= \frac{1}{\sqrt{3}}\langle L=1||T^{(1)}(\boldsymbol{d})||L_g=0\rangle.\end{aligned} \tag{A5}$$

Therefore, from (3), we have $k_g = 1/3$.

Similarly, for metastable qubits ($q = m$), inserting $L_q = 2$ and $J_q = 5/2$ to (A4) gives

$$\begin{aligned}\mu_m &= (-1)^{2I}\sqrt{(2I+4)(2I+6)(4)(6)} \\ &\quad\times\begin{pmatrix} I+\frac{3}{2} & 1 & I+\frac{5}{2} \\ -I-\frac{3}{2} & -1 & I+\frac{5}{2}\end{pmatrix}\begin{Bmatrix} \frac{3}{2} & I+\frac{3}{2} & I \\ I+\frac{5}{2} & \frac{5}{2} & 1\end{Bmatrix}\begin{Bmatrix} 1 & \frac{3}{2} & \frac{1}{2} \\ \frac{5}{2} & 2 & 1\end{Bmatrix}\langle L=1||T^{(1)}(\boldsymbol{d})||L_m=2\rangle \\ &= (-1)^{2I}\sqrt{(2I+4)(2I+6)(4)(6)}\times\frac{1}{\sqrt{2I+6}}\frac{(-1)^{2I+1}}{\sqrt{(2I+4)(6)}}\frac{(-1)}{\sqrt{20}}\langle L=1||T^{(1)}(\boldsymbol{d})||L_m=2\rangle \\ &= \frac{1}{\sqrt{5}}\langle L=1||T^{(1)}(\boldsymbol{d})||L_m=2\rangle.\end{aligned} \tag{A6}$$

From (3), we have $k_m = 1/5$.

Now we calculate α_f. Before we start, we introduce two useful identities for Wigner $3j$ and $6j$ symbols:

$$\sum_{m_1, m_2}\begin{pmatrix} j_1 & j_2 & j_3 \\ m_1 & m_2 & m_3\end{pmatrix}\begin{pmatrix} j_1 & j_2 & j_3' \\ m_1 & m_2 & m_3'\end{pmatrix} = \frac{\delta_{j_3, j_3'}\delta_{m_3, m_3'}}{2j_3+1}, \tag{A7}$$

$$\sum_{j_3}(2j_3+1)\begin{Bmatrix} j_1 & j_2 & j_3 \\ m_1 & m_2 & m_3\end{Bmatrix}\begin{Bmatrix} j_1 & j_2 & j_3 \\ m_1 & m_2 & m_3'\end{Bmatrix} = \frac{\delta_{m_3, m_3'}}{2m_3+1}. \tag{A8}$$

We start with the left-hand side of the first equation of (4) and apply the Wigner-Eckart theorem, which leads to

$$\begin{aligned}\sum_{F_f,M_f}|\langle L_e,J_e;F_e,M_e|\boldsymbol{d}|L_f,J_f;F_f,M_f\rangle|^2 &= \sum_{F_f}\left|\langle L_e,J_e;F_e||T^{(1)}(\boldsymbol{d})||L_f,J_f;F_f\rangle\right|^2\sum_{M_f}\left|\begin{pmatrix}F_f & 1 & F_e\\ -M_f & M_f-M_e & M_e\end{pmatrix}\right|^2\\ &= \sum_{F_f}\left|\langle L_e,J_e;F_e||T^{(1)}(\boldsymbol{d})||L_f,J_f;F_f\rangle\right|^2\sum_{M_f,s}\left|\begin{pmatrix}F_f & 1 & F_e\\ -M_f & s & M_e\end{pmatrix}\right|^2\\ &= \frac{1}{2F_e+1}\sum_{F_f}\left|\langle L_e,J_e;F_e||T^{(1)}(\boldsymbol{d})||L_f,J_f;F_f\rangle\right|^2,\end{aligned} \tag{A9}$$

where the last equality uses (A7). Applying (A2) with $J\to F$, $L\to J$, and $S\to I$ gives

$$\begin{aligned}\sum_{F_f,M_f}|\langle L_e,J_e;F_e,M_e|\boldsymbol{d}|L_f,J_f;F_f,M_f\rangle|^2 &= \frac{1}{2F_e+1}\sum_{F_f}(2F_e+1)(2F_f+1)\left|\begin{Bmatrix}J_e & F_e & I\\ F_f & J_f & 1\end{Bmatrix}\right|^2\left|\langle L_e,J_e||T^{(1)}(\boldsymbol{d})||L_f,J_f\rangle\right|^2\\ &= \left|\langle L_e,J_e||T^{(1)}(\boldsymbol{d})||L_f,J_f\rangle\right|^2\sum_{F_f}(2F_f+1)\left|\begin{Bmatrix}J_e & F_e & I\\ F_f & J_f & 1\end{Bmatrix}\right|^2\\ &= \frac{1}{2J_e+1}\left|\langle L_e,J_e||T^{(1)}(\boldsymbol{d})||L_f,J_f\rangle\right|^2,\end{aligned} \tag{A10}$$

where the last equality uses (A8). Applying (A2) gives

$$\sum_{F_f,M_f}|\langle L_e,J_e;F_e,M_e|\boldsymbol{d}|L_f,J_f;F_f,M_f\rangle|^2 = (2J_f+1)\left|\begin{Bmatrix}L_e & J_e & \frac{1}{2}\\ J_f & L_f & 1\end{Bmatrix}\right|^2\left|\langle L_e||T^{(1)}(\boldsymbol{d})||L_f\rangle\right|^2 \tag{A11}$$

Therefore, from (4), we obtain

$$\alpha(L_e,J_e,L_f,J_f) = (2J_f+1)\left|\begin{Bmatrix}L_e & J_e & \frac{1}{2}\\ J_f & L_f & 1\end{Bmatrix}\right|^2. \tag{A12}$$

Finally, inserting $L_e=1$ and $J_e=3/2$ gives the values of α_f shown in Table I.

APPENDIX B: Effects of metastable qubits' idling errors on QEC

Here we simulate how the idling errors of metastable qubits affect the QEC performance. Due to the finite lifetime of the $D_{5/2}$ states, metastable qubits can spontaneously decay to the $S_{1/2}$ manifold during idling. Such leakage errors can always be converted to erasures, using the erasure-conversion scheme described in Sec. II. The idling-error rate is given in (1), where the upper bound of time t is determined by the surface-code cycle time T, which can be considered as the clock time for fault-tolerant quantum computation.

We consider the example of metastable Ca^+ qubit in Table II, as its lifetime 1.16 s is significantly shorter than the metastable Ba^+ qubit's 30.14 s. In the surface-code simulations, similarly to Sec. V, we assume that all qubits can be erased, each with probability $p^{(\mathrm{idle})}(T)/4$ before each layer of CNOT gates, where the factor 1/4 is from the four layers of CNOT gates per cycle. Various values of surface-code cycle time T ranging from 3 ms to 1.19 s are considered, such that the idling-error rate $p^{(\mathrm{idle})}(T)/4$ is varied from 6.46×10^{-4} to 0.161. We also add two-qubit-gate errors of fixed rate $p^{(2q)}=1.14\times10^{-3}$ and measurement errors of fixed rate 10^{-4}, where the former is the lowest value considered in Fig. 3(a) for metastable Ca^+ qubits. The specific model for various types of two-qubit-gate errors is the same as in Sec. V.

Figure 5 shows the logical error rates p_L for various code distances d and idling-error rates $p^{(\mathrm{idle})}(T)/4$. The threshold idling-error rate is 5.14%, which is lower than the threshold two-qubit-gate error rate 6.13%, as there are more possible locations where errors can occur. As all idling errors are converted to erasures, a distance-d code is guaranteed to correct $d-1$ idling errors per cycle, as indicated by the slopes of the logical-error curves.

The top horizontal axis represents the surface-code cycle time T. While Fig. 5 plots the logical error rates for cycle times as long as ~ 1 s to show the threshold, such long cycle time is impractical for quantum computation. For relatively feasible cycle times, say, $T<10$ ms, p_L quickly decreases below 10^{-6} for $d\geq 5$. For $d=3$, p_L

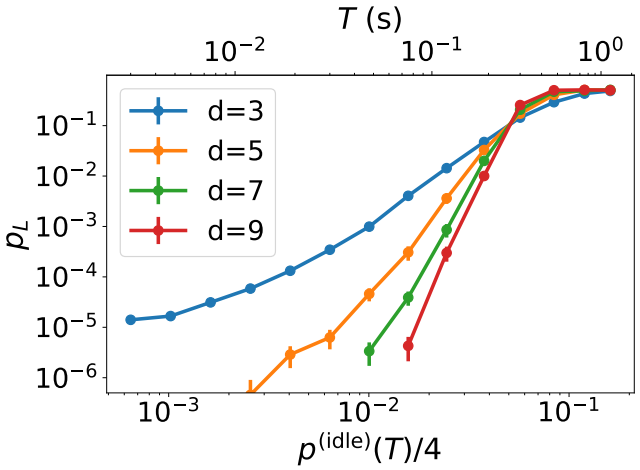

FIG. 5. Logical error rates of metastable Ca^+ qubits for various code distances d and idling-error rates $p^{(\mathrm{idle})}(T)/4$, where T is the surface-code cycle time, represented in the top horizontal axis. The factor 1/4 comes from the four layers of CNOT gates per cycle. Two-qubit-gate errors and measurement errors of fixed rate 1.14×10^{-3} and 10^{-4}, respectively, are added. The error bars represent the 95% confidence interval. The threshold idling-error rate is 5.14%, which corresponds to $T = 0.267$ s. We expect that significantly shorter cycle time, thus lower idling-error rate, is achievable.

converges to a nonzero value as the idling-error rate decreases, which indicates that the effects of the two-qubit-gate errors of fixed rate $p^{(2q)} = 1.14 \times 10^{-3}$ dominate the effects of the idling errors when $T \lesssim 3$ ms. Therefore, for reasonably short surface-code cycle times, we expect that the metastable qubits' idling errors have significantly smaller impact on the QEC performance than the gate errors. For metastable qubits with longer lifetime, such as Ba^+ and Yb^+, the idling errors will be even more negligible.

[1] E. Knill and R. Laflamme, Theory of quantum error-correcting codes, Phys. Rev. A **55**, 900 (1997).
[2] M. Mirrahimi, Z. Leghtas, V. V. Albert, S. Touzard, R. J. Schoelkopf, L. Jiang, and M. H. Devoret, Dynamically protected cat-qubits: a new paradigm for universal quantum computation, New Journal of Physics **16**, 045014 (2014).
[3] N. Ofek, A. Petrenko, R. Heeres, P. Reinhold, Z. Leghtas, B. Vlastakis, Y. Liu, L. Frunzio, S. Girvin, L. Jiang, *et al.*, Extending the lifetime of a quantum bit with error correction in superconducting circuits, Nature **536**, 441 (2016).
[4] S. Puri, L. St-Jean, J. A. Gross, A. Grimm, N. E. Frattini, P. S. Iyer, A. Krishna, S. Touzard, L. Jiang, A. Blais, S. T. Flammia, and S. M. Girvin, Bias-preserving gates with stabilized cat qubits, Science Advances **6**, eaay5901 (2020).
[5] I. Cong, H. Levine, A. Keesling, D. Bluvstein, S.-T. Wang, and M. D. Lukin, Hardware-efficient, fault-tolerant quantum computation with rydberg atoms, Phys. Rev. X **12**, 021049 (2022).
[6] P. Aliferis and J. Preskill, Fault-tolerant quantum computation against biased noise, Phys. Rev. A **78**, 052331 (2008).
[7] M. Li, D. Miller, M. Newman, Y. Wu, and K. R. Brown, 2d compass codes, Phys. Rev. X **9**, 021041 (2019).
[8] J. Guillaud and M. Mirrahimi, Repetition cat qubits for fault-tolerant quantum computation, Phys. Rev. X **9**, 041053 (2019).
[9] J. P. Bonilla Ataides, D. K. Tuckett, S. D. Bartlett, S. T. Flammia, and B. J. Brown, The XZZX surface code, Nat. Commun **12**, 2172 (2021).
[10] A. S. Darmawan, B. J. Brown, A. L. Grimsmo, D. K. Tuckett, and S. Puri, Practical quantum error correction with the XZZX code and kerr-cat qubits, PRX Quantum **2**, 030345 (2021).
[11] A. Dua, A. Kubica, L. Jiang, S. T. Flammia, and M. J. Gullans, Clifford-deformed surface codes, arXiv preprint arXiv:2201.07802 (2022).
[12] Q. Xu, N. Mannucci, A. Seif, A. Kubica, S. T. Flammia, and L. Jiang, Tailored XZZX codes for biased noise, arXiv preprint arXiv:2203.16486 (2022).
[13] M. Grassl, T. Beth, and T. Pellizzari, Codes for the quantum erasure channel, Phys. Rev. A **56**, 33 (1997).
[14] C. H. Bennett, D. P. DiVincenzo, and J. A. Smolin, Capacities of quantum erasure channels, Phys. Rev. Lett. **78**, 3217 (1997).
[15] C.-Y. Lu, W.-B. Gao, J. Zhang, X.-Q. Zhou, T. Yang, and J.-W. Pan, Experimental quantum coding against qubit loss error, Proceedings of the National Academy of Sciences **105**, 11050 (2008).
[16] G. Alber, T. Beth, C. Charnes, A. Delgado, M. Grassl, and M. Mussinger, Stabilizing distinguishable qubits against spontaneous decay by detected-jump correcting quantum codes, Phys. Rev. Lett. **86**, 4402 (2001).
[17] J. Vala, K. B. Whaley, and D. S. Weiss, Quantum error correction of a qubit loss in an addressable atomic system, Phys. Rev. A **72**, 052318 (2005).
[18] Y. Wu, S. Kolkowitz, S. Puri, and J. Thompson, Erasure conversion for fault-tolerant quantum computing in alkaline earth rydberg atom arrays, Nature Communications **13**, 4657 (2022).

[19] A. Kubica, A. Haim, Y. Vaknin, F. Brandão, and A. Retzker, Erasure qubits: Overcoming the T_1 limit in superconducting circuits, arXiv preprint arXiv:2208.05461 (2022).

[20] J. Ghosh, A. G. Fowler, J. M. Martinis, and M. R. Geller, Understanding the effects of leakage in superconducting quantum-error-detection circuits, Phys. Rev. A **88**, 062329 (2013).

[21] L.-A. Wu, M. S. Byrd, and D. A. Lidar, Efficient universal leakage elimination for physical and encoded qubits, Phys. Rev. Lett. **89**, 127901 (2002).

[22] M. S. Byrd, L.-A. Wu, and D. A. Lidar, Overview of quantum error prevention and leakage elimination, Journal of Modern Optics **51**, 2449 (2004).

[23] M. S. Byrd, D. A. Lidar, L.-A. Wu, and P. Zanardi, Universal leakage elimination, Phys. Rev. A **71**, 052301 (2005).

[24] A. G. Fowler, Coping with qubit leakage in topological codes, Phys. Rev. A **88**, 042308 (2013).

[25] J. Ghosh and A. G. Fowler, Leakage-resilient approach to fault-tolerant quantum computing with superconducting elements, Phys. Rev. A **91**, 020302 (2015).

[26] M. Suchara, A. W. Cross, and J. M. Gambetta, Leakage suppression in the toric code, in *2015 IEEE International Symposium on Information Theory (ISIT)* (2015) pp. 1119–1123.

[27] N. C. Brown and K. R. Brown, Comparing zeeman qubits to hyperfine qubits in the context of the surface code: $^{174}Yb^+$ and $^{171}Yb^+$, Phys. Rev. A **97**, 052301 (2018).

[28] N. C. Brown and K. R. Brown, Leakage mitigation for quantum error correction using a mixed qubit scheme, Phys. Rev. A **100**, 032325 (2019).

[29] N. C. Brown, M. Newman, and K. R. Brown, Handling leakage with subsystem codes, New Journal of Physics **21**, 073055 (2019).

[30] K. R. Brown, J. Kim, and C. Monroe, Co-designing a scalable quantum computer with trapped atomic ions, npj Quantum Information **2**, 1 (2016).

[31] P. Schindler, J. T. Barreiro, T. Monz, V. Nebendahl, D. Nigg, M. Chwalla, M. Hennrich, and R. Blatt, Experimental repetitive quantum error correction, Science **332**, 1059 (2011).

[32] D. Nigg, M. Mueller, E. A. Martinez, P. Schindler, M. Hennrich, T. Monz, M. A. Martin-Delgado, and R. Blatt, Quantum computations on a topologically encoded qubit, Science **345**, 302 (2014).

[33] N. M. Linke, M. Gutierrez, K. A. Landsman, C. Figgatt, S. Debnath, K. R. Brown, and C. Monroe, Fault-tolerant quantum error detection, Science advances **3**, e1701074 (2017).

[34] L. Egan, D. M. Debroy, C. Noel, A. Risinger, D. Zhu, D. Biswas, M. Newman, M. Li, K. R. Brown, M. Cetina, and C. Monroe, Fault-tolerant control of an error-corrected qubit, Nature **598**, 281 (2021).

[35] C. Ryan-Anderson, J. G. Bohnet, K. Lee, D. Gresh, A. Hankin, J. P. Gaebler, D. Francois, A. Chernoguzov, D. Lucchetti, N. C. Brown, T. M. Gatterman, S. K. Halit, K. Gilmore, J. A. Gerber, B. Neyenhuis, D. Hayes, and R. P. Stutz, Realization of real-time fault-tolerant quantum error correction, Phys. Rev. X **11**, 041058 (2021).

[36] C. Ryan-Anderson, N. C. Brown, M. S. Allman, B. Arkin, G. Asa-Attuah, C. Baldwin, J. Berg, J. G. Bohnet, S. Braxton, N. Burdick, J. P. Campora, A. Chernoguzov, J. Esposito, B. Evans, D. Francois, J. P. Gaebler, T. M. Gatterman, J. Gerber, K. Gilmore, D. Gresh, A. Hall, A. Hankin, J. Hostetter, D. Lucchetti, K. Mayer, J. Myers, B. Neyenhuis, J. Santiago, J. Sedlacek, T. Skripka, A. Slattery, R. P. Stutz, J. Tait, R. Tobey, G. Vittorini, J. Walker, and D. Hayes, Implementing fault-tolerant entangling gates on the five-qubit code and the color code, arXiv preprint arXiv:2208.01863 (2022).

[37] W. C. Campbell, Certified quantum gates, Phys. Rev. A **102**, 022426 (2020).

[38] D. T. C. Allcock, W. C. Campbell, J. Chiaverini, I. L. Chuang, E. R. Hudson, I. D. Moore, A. Ransford, C. Roman, J. M. Sage, and D. J. Wineland, omg blueprint for trapped ion quantum computing with metastable states, Applied Physics Letters **119**, 214002 (2021).

[39] H.-X. Yang, J.-Y. Ma, Y.-K. Wu, Y. Wang, M.-M. Cao, W.-X. Guo, Y.-Y. Huang, L. Feng, Z.-C. Zhou, and L.-M. Duan, Realizing coherently convertible dual-type qubits with the same ion species, Nature Physics , 1 (2022).

[40] H. Uys, M. J. Biercuk, A. P. VanDevender, C. Ospelkaus, D. Meiser, R. Ozeri, and J. J. Bollinger, Decoherence due to elastic rayleigh scattering, Phys. Rev. Lett. **105**, 200401 (2010).

[41] R. Ozeri, W. M. Itano, R. B. Blakestad, J. Britton, J. Chiaverini, J. D. Jost, C. Langer, D. Leibfried, R. Reichle, S. Seidelin, J. H. Wesenberg, and D. J. Wineland, Errors in trapped-ion quantum gates due to spontaneous photon scattering, Phys. Rev. A **75**, 042329 (2007).

[42] P. L. Knight, E. A. Hinds, M. B. Plenio, D. J. Wineland, M. Barrett, J. Britton, J. Chiaverini, B. DeMarco, W. M. Itano, B. Jelenković, C. Langer, D. Leibfried, V. Meyer, T. Rosenband, and T. Schätz, Quantum information processing with trapped ions, Philosophical Transactions of the Royal Society of London. Series A: Mathematical, Physical and Engineering Sciences **361**, 1349 (2003).

[43] A. Sørensen and K. Mølmer, Quantum computation with ions in thermal motion, Phys. Rev. Lett. **82**, 1971 (1999).

[44] Z. Zhang, K. J. Arnold, S. R. Chanu, R. Kaewuam, M. S. Safronova, and M. D. Barrett, Branching fractions for $P_{3/2}$ decays in ba^+, Phys. Rev. A **101**, 062515 (2020).

[45] A. Kreuter, C. Becher, G. P. T. Lancaster, A. B. Mundt, C. Russo, H. Häffner, C. Roos, J. Eschner, F. Schmidt-Kaler, and R. Blatt, Spontaneous emission lifetime of a single trapped ca^+ ion in a high finesse cavity, Phys. Rev. Lett. **92**, 203002 (2004).

[46] J. Jin and D. A. Church, Precision lifetimes for the Ca^+ 4p ^{2}P levels: Experiment challenges theory at the 1% level, Phys. Rev. Lett. **70**, 3213 (1993).

[47] R. Gerritsma, G. Kirchmair, F. Zähringer, J. Benhelm, R. Blatt, and C. Roos, Precision measurement of the branching fractions of the 4p $^2P_{3/2}$ decay of Ca II, The European Physical Journal D **50**, 13 (2008).

[48] Y. Wang, S. Crain, C. Fang, B. Zhang, S. Huang, Q. Liang, P. H. Leung, K. R. Brown, and J. Kim, High-fidelity two-qubit gates using a microelectromechanical-system-based beam steering system for individual qubit addressing, Phys. Rev. Lett. **125**, 150505 (2020).

[49] M. Cetina, L. Egan, C. Noel, M. Goldman, D. Biswas, A. Risinger, D. Zhu, and C. Monroe, Control of transverse motion for quantum gates on individually addressed atomic qubits, PRX Quantum **3**, 010334 (2022).

[50] M. Kang, Y. Wang, C. Fang, B. Zhang, O. Khosravani, J. Kim, and K. R. Brown, Designing filter functions of frequency-modulated pulses for high-fidelity two-qubit gates in ion chains, arXiv preprint arXiv:2206.10850

(2022).
[51] S. Jandura, J. D. Thompson, and G. Pupillo, Optimizing rydberg gates for logical qubit performance, arXiv preprint arXiv:2210.06879 (2022).
[52] K. R. Brown, J. Chiaverini, J. M. Sage, and H. Häffner, Materials challenges for trapped-ion quantum computers, Nature Reviews Materials **6**, 892 (2021).
[53] R. Raussendorf and J. Harrington, Fault-tolerant quantum computation with high threshold in two dimensions, Phys. Rev. Lett. **98**, 190504 (2007).
[54] A. G. Fowler, A. M. Stephens, and P. Groszkowski, High-threshold universal quantum computation on the surface code, Phys. Rev. A **80**, 052312 (2009).
[55] A. G. Fowler, M. Mariantoni, J. M. Martinis, and A. N. Cleland, Surface codes: Towards practical large-scale quantum computation, Phys. Rev. A **86**, 032324 (2012).
[56] Y. Tomita and K. M. Svore, Low-distance surface codes under realistic quantum noise, Phys. Rev. A **90**, 062320 (2014).
[57] S. Krinner, N. Lacroix, A. Remm, A. Di Paolo, E. Genois, C. Leroux, C. Hellings, S. Lazar, F. Swiadek, J. Herrmann, G. J. Norris, C. K. Andersen, M. Müller, A. Blais, C. Eichler, and A. Wallraff, Realizing repeated quantum error correction in a distance-three surface code, Nature **605**, 669 (2022).
[58] Y. Zhao, Y. Ye, H.-L. Huang, Y. Zhang, D. Wu, H. Guan, Q. Zhu, Z. Wei, T. He, S. Cao, F. Chen, T.-H. Chung, H. Deng, D. Fan, M. Gong, C. Guo, S. Guo, L. Han, N. Li, S. Li, Y. Li, F. Liang, J. Lin, H. Qian, H. Rong, H. Su, L. Sun, S. Wang, Y. Wu, Y. Xu, C. Ying, J. Yu, C. Zha, K. Zhang, Y.-H. Huo, C.-Y. Lu, C.-Z. Peng, X. Zhu, and J.-W. Pan, Realization of an error-correcting surface code with superconducting qubits, Phys. Rev. Lett. **129**, 030501 (2022).
[59] Google Quantum AI, Suppressing quantum errors by scaling a surface code logical qubit, arXiv preprint arXiv:2207.06431 (2022).
[60] D. M. Debroy, M. Li, S. Huang, and K. R. Brown, Logical performance of 9 qubit compass codes in ion traps with crosstalk errors, Quantum Science and Technology **5**, 034002 (2020).
[61] A. M. Steane, Active stabilization, quantum computation, and quantum state synthesis, Phys. Rev. Lett. **78**, 2252 (1997).
[62] E. Dennis, A. Kitaev, A. Landahl, and J. Preskill, Topological quantum memory, Journal of Mathematical Physics **43**, 4452 (2002).
[63] N. Delfosse and N. H. Nickerson, Almost-linear time decoding algorithm for topological codes, Quantum **5**, 595 (2021).
[64] S. Huang and K. R. Brown, Fault-tolerant compass codes, Phys. Rev. A **101**, 042312 (2020).
[65] C. Gidney, Stim: a fast stabilizer circuit simulator, Quantum **5**, 497 (2021).
[66] O. Higgott, Pymatching: A python package for decoding quantum codes with minimum-weight perfect matching, ACM Transactions on Quantum Computing **3**, 1 (2022).
[67] C. Gidney, How do I perform an erasure error in stim?, `https://quantumcomputing.stackexchange.com/questions/26582`, accessed: 2022-10-02.
[68] D. Schwerdt, Y. Shapira, T. Manovitz, and R. Ozeri, Comparing two-qubit and multiqubit gates within the toric code, Phys. Rev. A **105**, 022612 (2022).
[69] A. J. Rasmusson, M. D'Onofrio, Y. Xie, J. Cui, and P. Richerme, Optimized pulsed sideband cooling and enhanced thermometry of trapped ions, Phys. Rev. A **104**, 043108 (2021).
[70] J. E. Christensen, D. Hucul, W. C. Campbell, and E. R. Hudson, High-fidelity manipulation of a qubit enabled by a manufactured nucleus, npj Quantum Information **6**, 1 (2020).
[71] A. Ransford, C. Roman, T. Dellaert, P. McMillin, and W. C. Campbell, Weak dissipation for high-fidelity qubit-state preparation and measurement, Phys. Rev. A **104**, L060402 (2021).
[72] M. Kang, Q. Liang, M. Li, and Y. Nam, Efficient motional-mode characterization for high-fidelity trapped-ion quantum computing, arXiv preprint arXiv:2206.04212 (2022).